Modeling the dynamic fracture in concrete: an eigensoftening meshfree approach

Pedro Navas[a], Rena C. Yu[*,a], Bo Li[b], Gonzalo Ruiz[a]

[a] E. T. S. de Ingenieros de Caminos, C. y P., Universidad de Castilla-La Mancha, Ciudad Real 13071, Spain
[b] Dept. of Mechanical and Aerospace Engineering, Case Western Reserve University, Cleveland, Ohio 44106, USA

ARTICLE INFO

ABSTRACT

The objective of this work is twofold. First, we develop an eigensoftening algorithm to capture the gradual process of failure in materials with a softening behavior as an extension of the eigenerosion approach. Both methods are validated against the physical measurements in three-point bending tests of concrete with a drop-weight device, including impact and reaction forces, loading-line displacements as well as strain histories from gauges. The comparison shows that the eigenerosion algorithm significantly overestimates the tensile stresses and the strain peaks, while it captures the forces and crack pattern accurately. Predictions made by the proposed eigensoftening algorithm agree very well with experimental results in all aspects. Second, the energy evolution and partition in the beam predicted by the eigensoftening algorithm at various impact rates is analyzed to quantify the rate dependent fracture properties of concrete. It is demonstrated that, at impact loading conditions, the area below the reaction-deflection curve is much larger than the dissipated fracture energy.

1. Introduction

The rate effect on fracture propagation in concrete with or without reinforcements has been the centre of interest for the last three decades, from both experimental and numerical standpoints. Within the framework of finite element methods, typical techniques to capture crack propagation vary from employing cohesive approaches [1,2] by adaptively inserting cohesive elements [3–5] at solid element boundaries to adopting crack band theory [6] or handling arbitrary crack paths by level set representation of the fracture surface [7,8]. Within the scenario of meshfree methods, the visibility criterion [9] or particle erosion [10–13] have been opted for to reproduce fracture propagation. In the current work, we attempt to model the dynamic fracture propagation in high-strength concrete (HSC) employing the optimal transportation meshfree (OTM) approximation scheme [12–15]. Such a scheme is chosen for its numerous advantages such as the exact mass transport, the satisfaction of the continuity equation, exact linear and angular momentum conservation. Since the deformation and velocity fields are interpolated from nodal values using shape functions based on the principle of maximum entropy, the Kronecker-delta property at the boundary makes it possible for the direct imposition of essential boundary conditions.

Regarding fracture, we first assess the applicability of an eigenerosion algorithm to quasi-brittle materials such as concrete. The

eigenerosion approach to brittle fracture was developed by Pandolfi et al. [11,12]. They approximate the crack set by means of eigen-deformations, which enable the material to develop displacement jumps at no cost of local elastic energy. The erosion of the material means that each material point can be either intact or be completely failed or eroded and has no load bearing capacity. Even though the method has been successfully applied to dynamic fragmentation of metals, quantitative validations, such as stress or strain levels near or at the crack set compared to experimental measures, are still lacking.

Having in mind that the eigenerosion approach was intended for perfectly brittle fracture, an *eigensoftening* concept is developed for quasi-brittle materials. This is engineered for the gradual rather than abrupt dissipation of the fracture energy. In other words, the material softens in a progressive manner until its complete failure (i.e. the formation of a stress-free crack). This is equivalent to the crack band model [6], since energy dissipation is through the softened (or failed) volume. In the meantime, the analogy to cohesive approaches is straightforward through the definition of a damage variable. Furthermore, the implementation follows the same procedure as that of the eigenerosion algorithm except for the strength criterion for crack initiation. Consequently, the current work emerges as the first alternative which combines the advantages of the three methods for the fracture quasi-brittle materials, and particularly suitable for a meshfree framework.

Moreover, the quantification of fracture energy is of great interest under dynamic loading. From the experimental part, in 1980s, using high speed photography, Mindess and Bentur [16] carried out studies of the fracture, under impact loading, for both plain and fibre reinforced concrete, as well as those with conventional reinforcement. They concluded that the cracking process under impact loading is not substantially different from that which occurs under static loading, even though the absorption of energy is quantitatively different due to the inertia effect. In a sequel, Mindess, Banthia and Yan [17] showed that both the fracture toughness and the fracture energy were dramatically increased under impact loading. Banthia et al. [18] also presented a drop-weight impact-testing machine for generating impact flexural loading; by replacing the distributed inertia load with a generalized point inertial load and subtracting it from the tup load, they obtained the true bending load, when plotted with respect to the load-point deflection, the area below was considered as the dynamic fracture energy. This same procedure, which we term the *Hypothesis of Banthia et al.*, has been widely employed by Banthia, Mindess and co-workers [19–21], and recently by Ruiz and coworkers [22–25]. However, except the analytic demonstration by Banthia et al. [18] with significant simplification, neither the validity of such a procedure nor the derived fracture energy has been rigorously verified. By explicitly representing both the projectile and the target without making simplifications, we aim to quantify the dynamic fracture energy and probe the validity of the assumptions assumed by Banthia et al. through numerical simulations.

Next the experimental setup and observations are presented. The meshfree methodology, eigenerosion and eigensoftening algorithms for fracture are described in Section 3. Numerical results are given in Section 4. Finally, relevant conclusions are drawn in Section 5.

2. Experimental observations

In order to study the loading-rate effect in concrete, a drop-weight impact instrument [24], see Fig. 1, was designed and constructed in the Laboratory of Materials and Structures at the University of Castilla-La Mancha. Three-point bending tests on notched beams were conducted

under impact loading. It has the capacity to drop a mass maximum of 316 kg from heights of up to 2.6 m, and can accommodate flexural specimens with spans of up to approximately 1.6 m. In the study of Zhang et al. [22,23], an impact hammer of 120.6 kg was employed to drop from three different heights, 360, 160 and 40 mm with the corresponding impact speeds of 2640, 1760 and 881 mm/s, respectively. The impact force was measured by a piezoelectric force sensor. In addition, the reaction force was determined by two force sensors located between the support and the specimen. A strain amplifier and two oscilloscopes were used to acquire the data from the strain gauges, located as it can be seen in Fig. 1.

The beam dimensions were 100 mm × 100 mm (B × D) in cross section, and 420 mm in total length (L). The initial notch-depth ratio was approximately 0.5, and the span, S, was fixed at 300 mm during the tests, see Fig. 1. The specimen surface was polished and all four strain gauges were bonded to that surface, with a distance of 10 mm between neighboring gauges. The four strain gauges were bonded 10 mm apart from the centerline of the beam, see Fig. 1. Consequently, both strain history at the bonded positions, and the time at which the crack tip reaches each strain gauge [23] were obtained.

The material was characterized with independent tests and the measured material properties, such as the material density, ρ, compressive strength, f_c, the tensile strength, f_t, the specific fracture energy, G_F and the elastic modulus, E, are given in Table 1.

3. The meshfree methodology

For completeness, we first summarize the basics of the OTM scheme, the eigen-erosion algorithm to treat brittle fracture within the meshfree framework. Subsequently, the eigen-softening algorithm, particularly designed for fracture of quasi-brittle materials within the OTM framework is developed in detail.

3.1. The OTM scheme

OTM [14] is a meshfree updated Lagrangian numerical scheme that combines concepts from optimal transportation theory with a material-
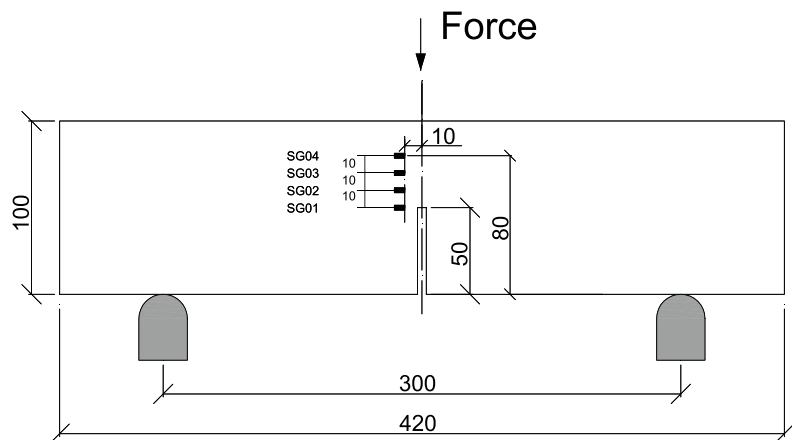
(a)   (b)

Fig. 1. (a) The drop-weight machine designed at the Laboratory of Materials and Structures, University of Castilla-La Mancha [24]. (b) Geometry and dimension of the concrete beam (in mm) and location of the strain gauges [23].

Table 1
Mechanical properties of the high strength concrete tested by Zhang et al. [23].

	ρ (kg/m³)	f_c (MPa)	f_t (MPa)	G_F (N/m)	E (GPa)	d_{max} (mm)
Mean	2368	102.7	5.4	141	31	12
Std. Dev	1	2	0.8	9	2	-
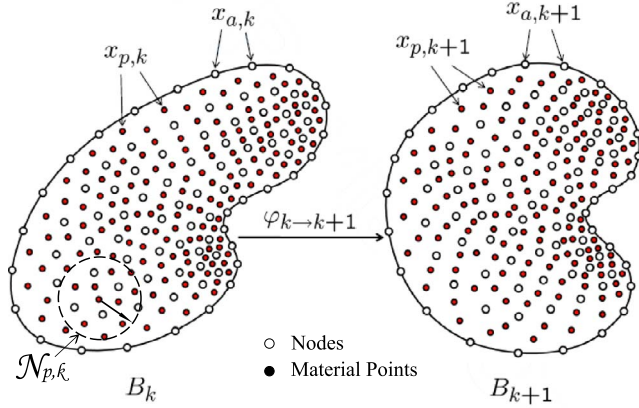
Fig. 2. Schematic of the OTM approximation scheme showing the incremental motion from time t_k to t_{k+1} and the corresponding sets of nodal points (empty circles), $x_{a,\,k}$ and $x_{a,k+1}$, and material points (solid circles), $x_{p,\,k}$ and $x_{p,k+1}$, respectively.
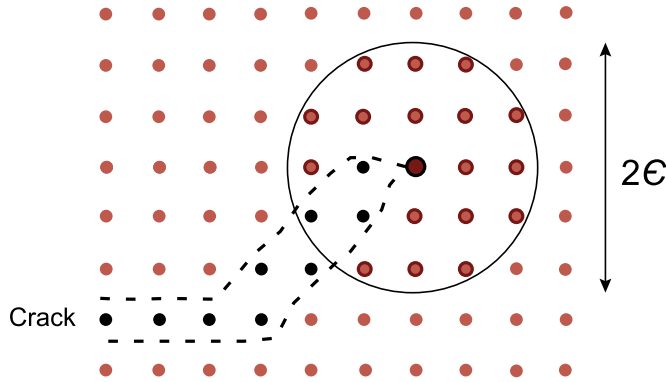

Fig. 3. Scheme of a crack (black dots) as set of failed material points, and of the ϵ-neighborhood (inside the circle) of the material point located at the crack tip (red dots). (For interpretation of the references to colour in this figure legend, the reader is referred to the web version of this article.)

point sampling and the local max-ent meshfree approximation [26]. The method has been used in applications involving dynamic deformation and failure of materials with excellent results. The numerous advantages previously mentioned ensure its robustness and stability in numerical calculations.

Two sets of points, namely, nodal points and material points are introduced in the OTM method. A schematic of the OTM approximation scheme for an incremental motion from time t_k to t_{k+1} is shown in Fig. 2.

The kinematic information of the domain, such as the displacement, velocity and acceleration field, is stored at the nodes. The material responses and local state variables are evaluated at the material points, which are also transported by the incremental motion of the domain. To approximate the incremental motion from nodal displacement field, the local max-ent approximation scheme defined by Arroyo and Ortiz [26] is employed. The local max-ent function (LME), as a Pareto set, is optimal for $\beta \in (0, \infty)$ and obtained as

$$N_a(\mathbf{x}) = \frac{\exp[-\beta \, |\mathbf{x}-\mathbf{x_a}|^2 + \lambda^* \cdot (\mathbf{x} - \mathbf{x_a})]}{Z(\mathbf{x}, \lambda^*(\mathbf{x}))}, \tag{1}$$
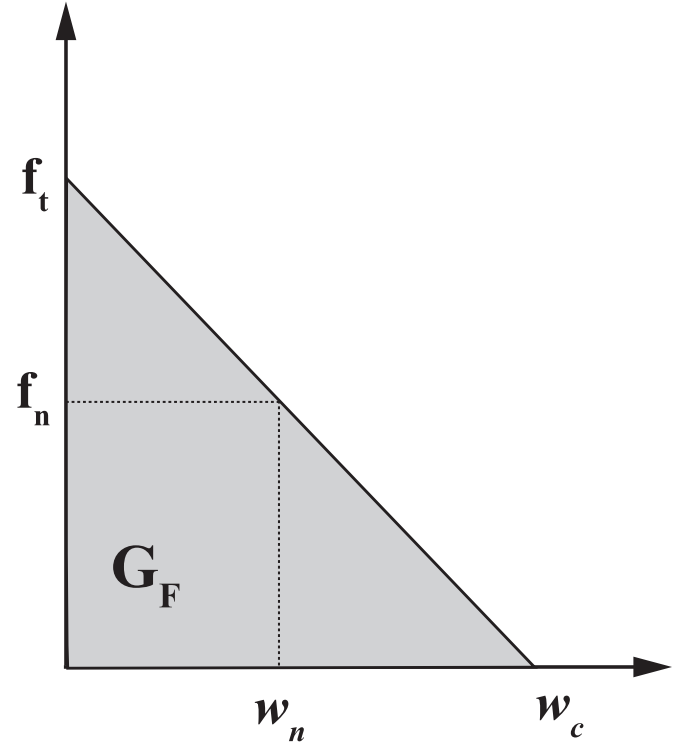

Fig. 4. Scheme of a linear cohesive law, where the shade area is G_F, f_t is the tensile strength, and w_c is the critical opening displacement.

where

$$Z(\mathbf{x}, \lambda) = \sum_{a=1}^{n} \exp[-\beta \, |\mathbf{x} - \mathbf{x_a}|^2 + \lambda \cdot (\mathbf{x} - \mathbf{x_a})], \tag{2}$$

being $\lambda^*(\mathbf{x})$ the unique minimizer for $\log Z(\mathbf{x}, \lambda)$. The parameter β is related with the discretization size (or nodal spacing), h, whereas γ controls the locality of the shape functions, as follows

$$\beta = \frac{\gamma}{h^2}. \tag{3}$$

For a uniform nodal spacing, β is also a constant, thus the first derivatives can be obtained by employing the following expression

$$\nabla N_a^* = -N_a^* (\mathbf{J}^*)^{-1} (\mathbf{x} - \mathbf{x_a}), \tag{4}$$

where $\mathbf{J}$ is the Hessian matrix, defined by

$$\mathbf{J}(\mathbf{x}, \lambda, \beta) = \frac{\partial \mathbf{r}}{\partial \lambda}, \tag{5}$$

$$\begin{aligned} \mathbf{r}(\mathbf{x}, \lambda, \beta) &\equiv \partial_\lambda \log Z(\mathbf{x}, \lambda) \\ &= \sum_a N_a(\mathbf{x}, \lambda, \beta)(\mathbf{x} - \mathbf{x_a}). \end{aligned} \tag{6}$$

Note that the objective of the above procedure is to find the λ which minimizes $\log Z(\mathbf{x}, \lambda)$. This unconstrained minimization problem with a strictly convex objective function can be solved efficiently and robustly by a combination of the Newton–Raphson method and Nelder–Mead Simplex algorithm [26,27].

In calculations, the max-ent shape functions are reconstructed continuously from the nodal set, which changes in every step by adapting to the local deformation of the material points. This overcomes the essential difficulties of mesh entanglement that arise in Lagrangian grid-based numerical schemes. On the other hand, material points result from the spatial approximation of the mass densities $\rho_{h,\,k}(x)$ by M points
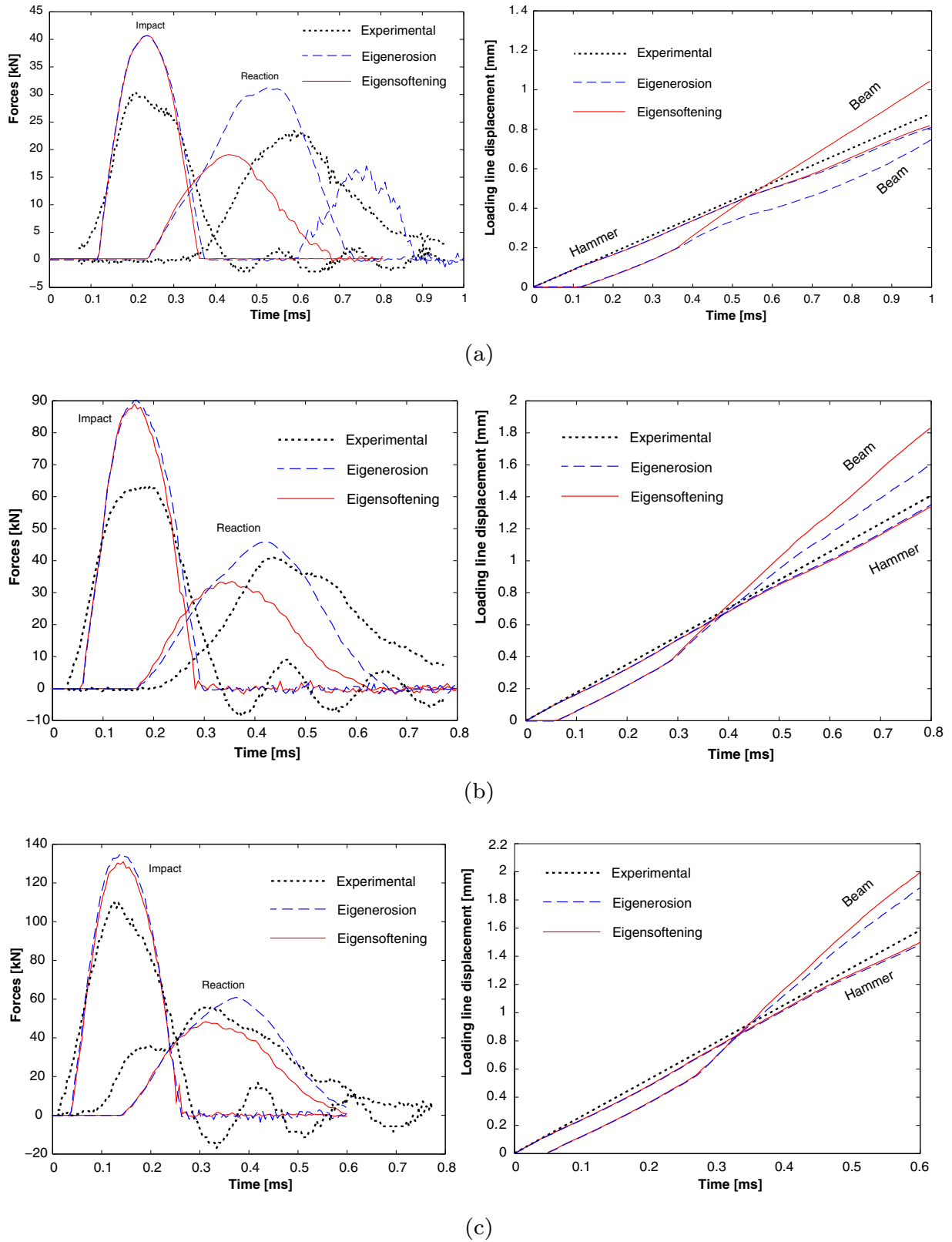
Fig. 5. Comparison between experimental and computational impact and reaction forces (left) and impact-line displacements (right) for (a) 881 mm/s; (b) 1760 mm/s; and (c) 2640 mm/s.

$$\rho_{h,k}(x) = \sum_{p=1}^{M} m_p \delta(x - x_{p,k}),$$

(7)

where $x_{p,\ k}$ represents the position at time t_k of material point p, m_p is the mass of the material point and $\delta(x - x_{p,k})$ is the Dirac-delta distribution centered at $x_{p,\ k}$. Material points are convected by the deformation and carry a fixed mass as well as serve the purpose of integration points for the calculation of the effective nodal forces and masses. The spatial discretization is completed by approximating the deformation mapping as
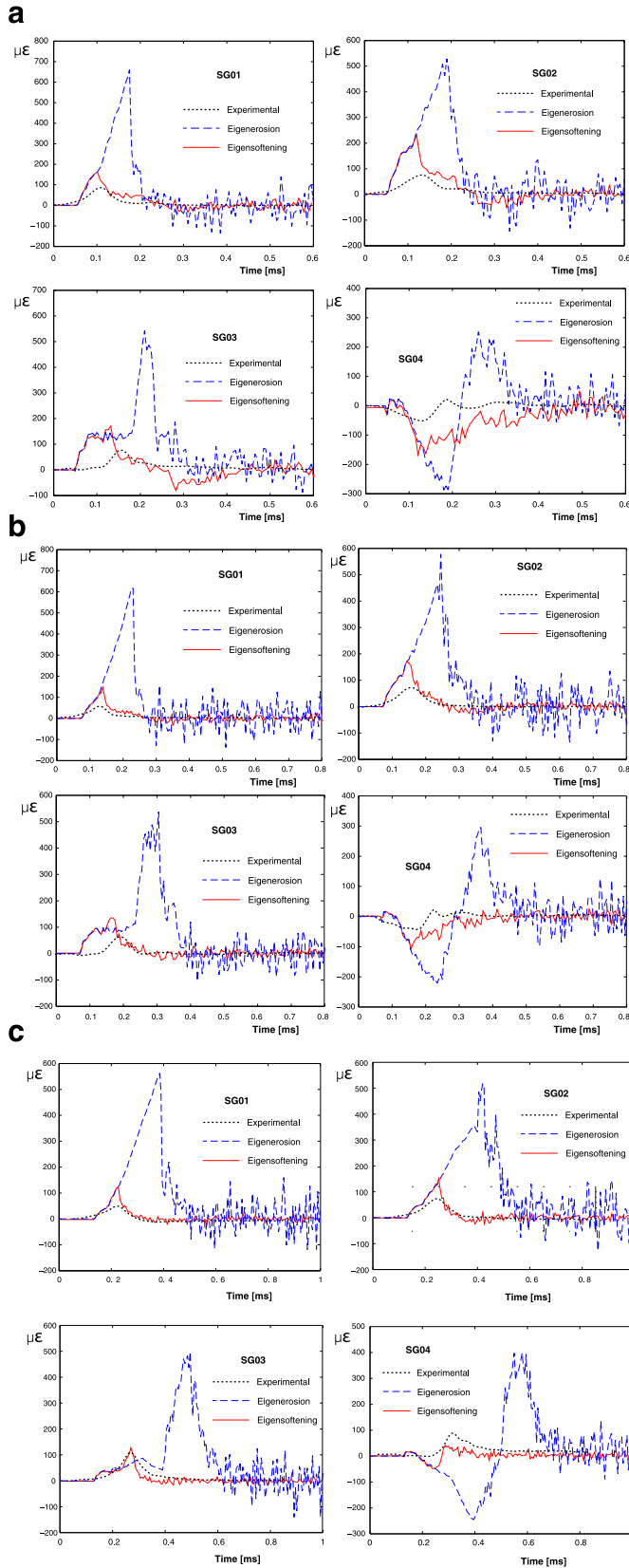
Fig. 6. Numerically obtained strain evolution at the same locations where the four strain gauges are bonded and the crack-front position with respect to time for (a) 2640 mm/s; (b) 1760 mm/s; and (c) 881 mm/s.

$$\varphi_{h,k\to k+1}(x) = \sum_{a=1}^{N} x_{a,k+1} N_{a,k}(x) \tag{8}$$

where $x_{a,k+1}$ is the position of node a at time t_{k+1}, and $N_{a,\ k}(x)$ are max-ent shape functions defined over the configuration for node a at time t_k. The interpolation at a material point $x_{p,\ k}$ depends solely on the nodes contained in a small local neighborhood $N_{p,\ k}$ as shown in Fig. 2. The reconstruction of the local neighborhoods leads to a new reconnection of the material points and the nodal set on the fly adaptively.

3.2. Eigenerosion algorithm

Within the context of OTM formulation, fracture can be modelled simply by failing material points according to an energy-release criterion. When the material points are failed, they are neglected from the computation of stresses in the model, which approximates the presence of cracks, this is the eigen-erosion algorithm developed by Pandolfi and Ortiz [11]. Next we compute the energy-release rate attendant to the failure of material point p as is it seen in [10–12,15].

$$G_{p,k+1} = \frac{C\epsilon}{m_{p,k+1}} \sum_{x_{q,k+1}\in B_\epsilon(x_{p,k+1})} m_q W_k(F_{q,k+1}),$$
$$m_{p,k+1} = \sum_{x_{q,k+1}\in B_\epsilon(x_{p,k+1})} m_q, \tag{9}$$

where $B_\epsilon(x_{p,k+1})$ is the sphere of radius ϵ centered at $x_{p,k+1}$ known as the ϵ-neighborhood of the material point, $m_{p,k+1}$ is the mass of the neighborhood at loading step $k+1$, $W_k(F_{q,k+1})$ is the current free-energy density per unit mass at the material point $x_{q,k+1}$ and C is a normalizing constant. A scheme of the configuration of the ϵ-neighborhood is plotted in Fig. 3.

The material point is failed when $G_{p,k+1}$ surpasses a critical energy release rate that measures the material-specific energy, G_F, required to create a fracture surface of unit area. In calculations, the failed material-point set is updated at every time step according to this criterion. For linear elasticity, Schmidt et al. [10] have shown that this approximation converges to Griffith fracture in the limit of an infinitely fine discretization. In order to minimize the computational effort, employing an averaging over an intermediate ϵ-neighborhood to compute the energy-release rate attendant to material-point failure, Eq. (9), is essential to convergence. Indeed, erosion schemes that estimate the energy-release rate based on the energy of a single material point suffer from mesh-dependency and may overestimate the toughness of the material. It needs to be pointed out that when a material point satisfies the erosion condition, its contribution to the internal force vector and to the material stiffness matrix is set to zero, but its contribution to the mass matrix is maintained. The mass of a material point is discarded only when an eroded material point is not connected to any nodes.

3.3. Eigensoftening algorithm

From different numerical simulations carried out using the eigen-erosion algorithm for modeling fracture in concrete (see next Section), the main drawback observed is the over intensification of tensile stresses near the crack tip. This fact leads to an unrealistic stress concentration, reaching values significantly higher than the tensile strength of quasi-brittle materials. This is attributed to the fact that an energetic criterion is adopted in the eigenerosion algorithm. In order for a material point to be eroded, the strain energy accumulated must reach the given value, G_F. Such an energy accumulation is necessarily obtained through higher values of stresses (and strains) in quasi-brittle materials. In the limit case, infinitely high stresses will be reached, such is the case of infinite stress concentration at the crack tip in Linear Elastic Fracture Mechanics. To overcome this limitation, we propose the concept of *eigensoftening* to take into account the gradual failure in quasi-brittle materials. This is similar to that of cohesive fracture. For instance, in
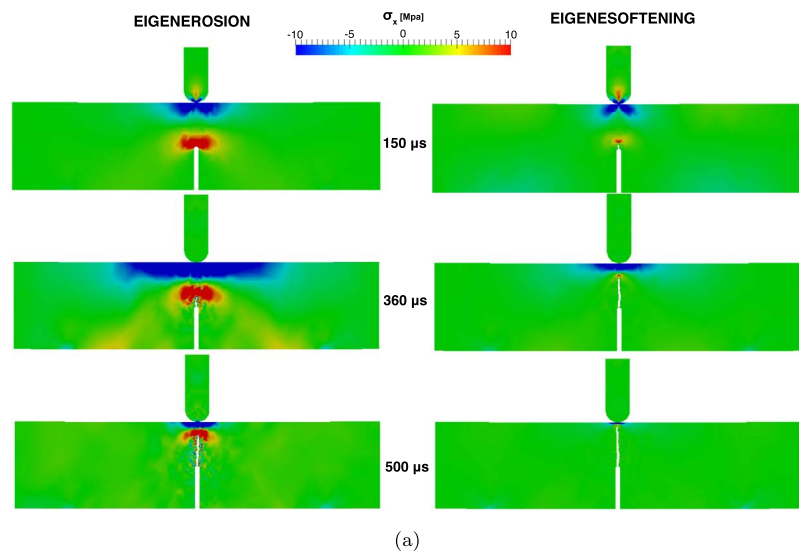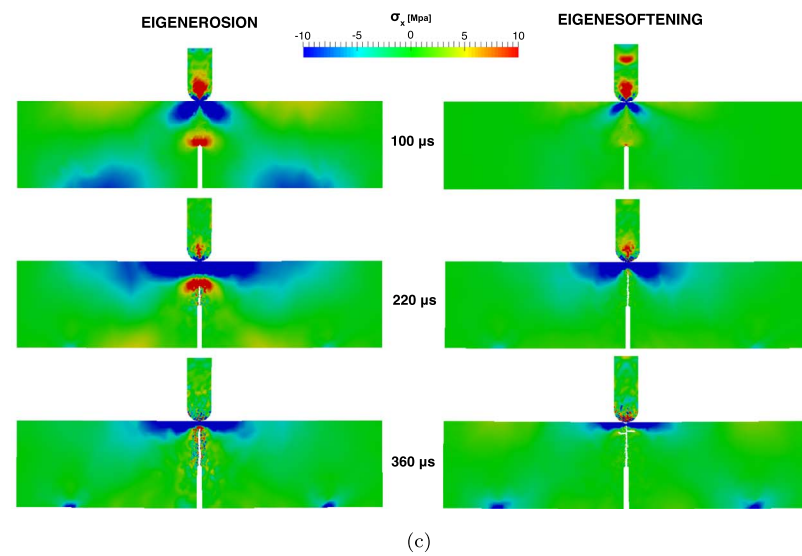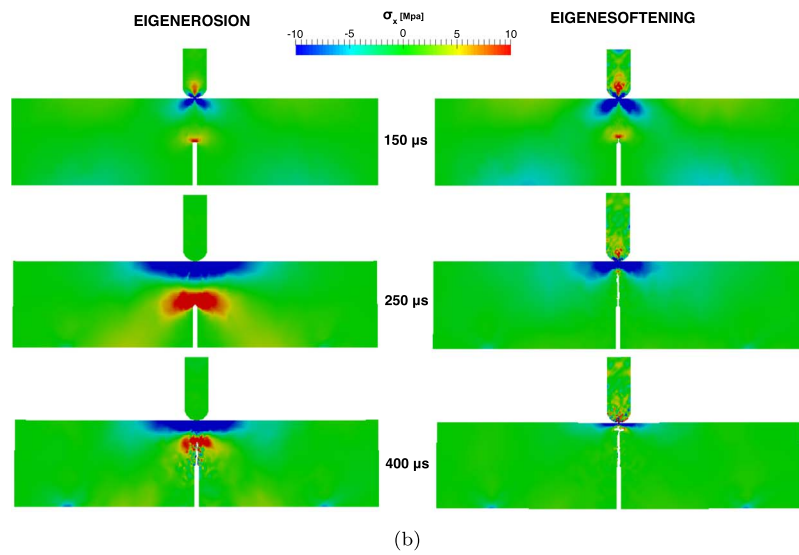
Fig. 7. Evolution of the stresses for eigenerosion and eigensoftening approaches for (a) 881 mm/s; (b) 1760 mm/s; and (c) 2640 mm/s.
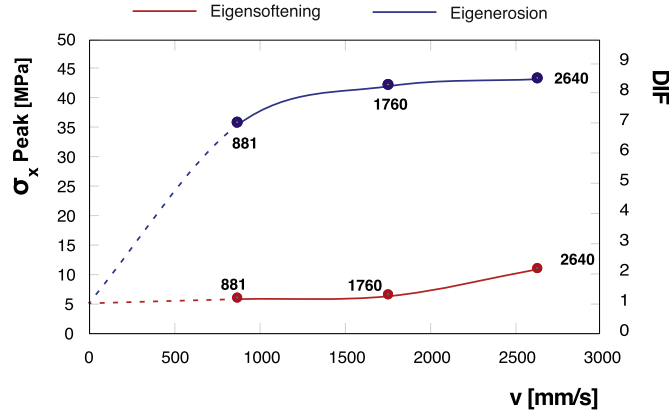
Fig. 8. Peak values of the tensile stresses and the corresponding DIFs for different loading velocities calculated with eigenerosion and eigensoftening models.

Table 2
Dynamic Increase Factor (DIF) for tensile strength and fracture energy obtained from the eigensoftening calculations.

Impact Velo. [mm/s]	σ_{max} [MPa]	DIF -	Diss. Energy [J]	DIF -
881	5.8	1.14	0.75	1.06
1760	6.3	1.24	1.00	1.41
2640	10.9	2.13	1.50	2.12

Fig. 4, a linear decreasing cohesive law is plotted, where the shaded area represents the static fracture energy per unit of area, G_F. When the maximum tensile strength, f_t, is reached, a cohesive crack is formed with zero opening displacement. Once the opening displacement, w, reaches a critical vale, w_c, a stress-free crack is attained. For intermediate values, w_n, a damage value between zero and one represents the extension to which the material has failed.

The implementation of the eigensoftening algorithm consists in adopting a strength criterion for crack initiation and a softening law which is proper to the material under study before the formation of a stress-free crack. Following the philosophy of eigenerosion, we rewrite Eq. (9) in terms of the principal stresses at time t_{k+1}. In specific, we consider the maximum principal stress theory for brittle fracture. To this end, the variation of the averaged strain energy density in the ϵ-neighborhood of the material point $x_{p,k+1}$ can be expressed as,

$$\delta W_p^\epsilon = \frac{\partial G_p}{C\epsilon} = \frac{1}{m_p} \sum_{x_q \in B_\epsilon(x_p)} m_q \sigma_{q,1} \delta \epsilon_q \tag{10}$$

where $\sigma_{q,1}$ is the maximum principal stress at a neighboring material point $x_{q,k+1}$ for a general three dimensional problem. We introduce here an effective strain ϵ_q at the material point $x_{q,k+1}$, such that the variation of the local strain energy can be obtained as $\delta W_q = \sigma_{q,1} \delta \epsilon_q$. In addition, assume the effective strain increment of each material point at every time step can be approximated by its counterpart in the neighborhood. This is due to the fact that there is no significant variation when the space discretization is small enough. Consequently, Eq. (10) is simplified as follows,

$$\delta W_p^\epsilon = \frac{\delta \epsilon_p}{m_p} \sum_{x_{q,k+1} \in B_\epsilon(x_{p,k+1})} m_q \sigma_{q,1}. \tag{11}$$

With the definition of an equivalent critical stress at the material point $x_{p,k+1}$:

$$\sigma_p^\epsilon = \frac{1}{m_p} \sum_{x_{q,k+1} \in B_\epsilon(x_{p,k+1})} m_q \sigma_{q,1}$$

where $m_p = \sum_{x_{q,k+1} \in B_\epsilon(x_{p,k+1})} m_q$, $\tag{12}$

we obtain the conjugate relationship between the equivalent critical stress and the averaged strain energy density, i.e., $\delta W_p^\epsilon = \sigma_p^\epsilon \delta \epsilon_p$. Once the first principal stress, the maximum eigenvalue of the Cauchy stress tensor, is determined for every intact material point, its average over an ϵ-neighborhood defined in Eq. (12) can be easily calculated. When $\sigma_{p,k+1}^\epsilon$ surpasses the tensile strength, f_t, the softening behavior is activated, which in turn causes a reduction of the internal forces as follows,

$$f^{int} = (1-\chi) \sum^p \int_\Omega \sigma_{p,k+1} \nabla N dV, \tag{13}$$

where χ is the damage variable, ranges between zero (an intact material) and one (completely failed material points). For the case of a linear softening behavior described in Fig. 4, it is calculated as,

$$1 - \chi = \frac{f_n}{f_t} = 1 - \frac{w_n}{w_c} \longrightarrow \chi = \frac{w_n}{w_c} \tag{14}$$

Since the energy dissipation is within a volume rather than a surface as the case of cohesive fracture, a band with, h_ϵ, equivalent to the crack band model of Bažant [6] is introduced. The effective fracture strain, ϵ_f^ϵ, defined as the difference between the strain at crack initiation, $\epsilon_1(x_{p,\,0})$, and the current strain, $\epsilon_1(x_{p,k+1})$, for material point p. At the same time, ϵ_f^ϵ can also be represented as the current crack opening w_n within the band width, h_ϵ. Consequently,

$$\epsilon_f^\epsilon = \epsilon_1(x_{p,k+1}) - \epsilon_1(x_{p,0}) = \frac{w_n}{h^\epsilon} \tag{15}$$

Combing Eqs. (14) and (15), the damage variable can be computed as

$$\chi = \frac{\epsilon_f^\epsilon h^\epsilon}{w_c} \tag{16}$$

for a linear softening behavior. For a generic softening behavior, the damage variable can be expressed in terms of the following variables,

$$\chi = \chi(\epsilon_f^\epsilon, h^\epsilon, f_t, w_c, G_f). \tag{17}$$

It bears emphasis that a reference value for h^ϵ is between two and four times the maximum size of the aggregates for concrete according to Bažant [28].

4. Numerical results and discussion

In this Section, we compare the results obtained with the aforementioned methodologies on the simulation of the dynamic fracture propagation in a three-point-bend beam impacted by a drop-weight device in a 2D setting. Both the projectile (the hammer) and the target (the concrete beam) are explicitly represented. Several levels of discretization are employed to assess the objectiveness of the obtained results. The results obtained in this Section are from a discretization of 3980 nodes, 7534 material points, and a nodal spacing of 0.65 mm near the middle section is maintained.

First we validate the reaction and impact forces as well as the load-line displacement against their experimental counterparts, the strain evolutions are compared with those measured from strain gauges. Next the horizontal stress distributions, crack front evolutions and crack propagation velocities are extracted. Finally the energy evolution is assessed. All the results are presented for the three different experimental loading velocities.

4.1. Validation against experimental results

Since the impact forces applied by the hammer and the reaction forces at the two supports were experimentally measured, they are
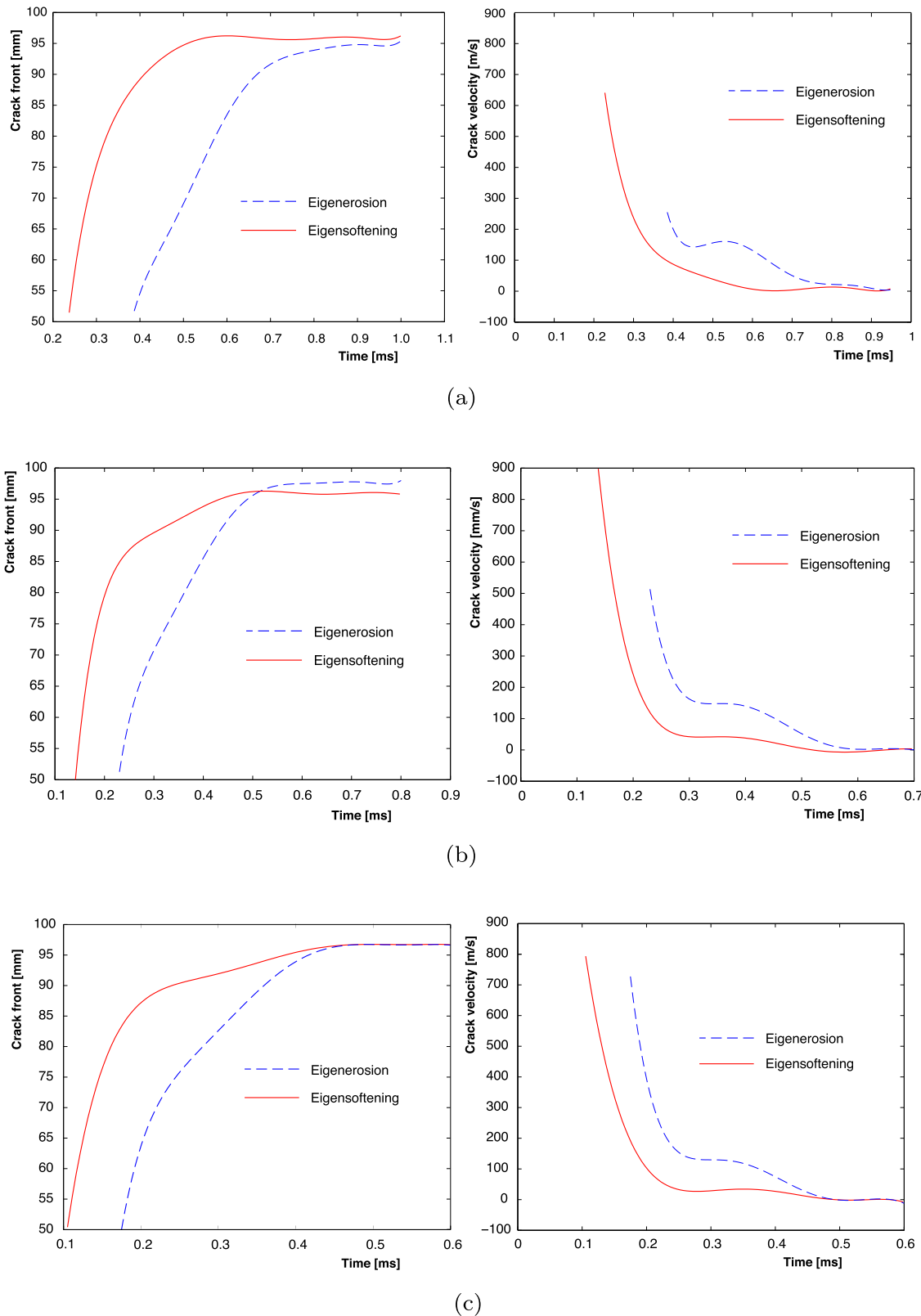
Fig. 9. Crack front position (left column) and crack front velocity (right column) for both eigenerosion and eigensoftening models for (a) 881 mm/s; (b) 1760 mm/s; and (c) 2640 mm/s.

compared with the numerical ones in Fig. 5 for the different impact velocities. Note that the general trend of both forces are correctly captured with both methods. However, lower reaction values are observed in the eigensoftening results compared to those of eigenerosion, since the fracture occurs earlier. Additionally plotted in Fig. 5 are the

recorded impact-line displacements contrasted with the numerical ones. The displacement of the hammer fits quite well with the experimental measurement. Nevertheless, a discrepancy in displacements between the hammer and the top centerline of the beam is observed when eigensoftening is employed. This indicates a separation between
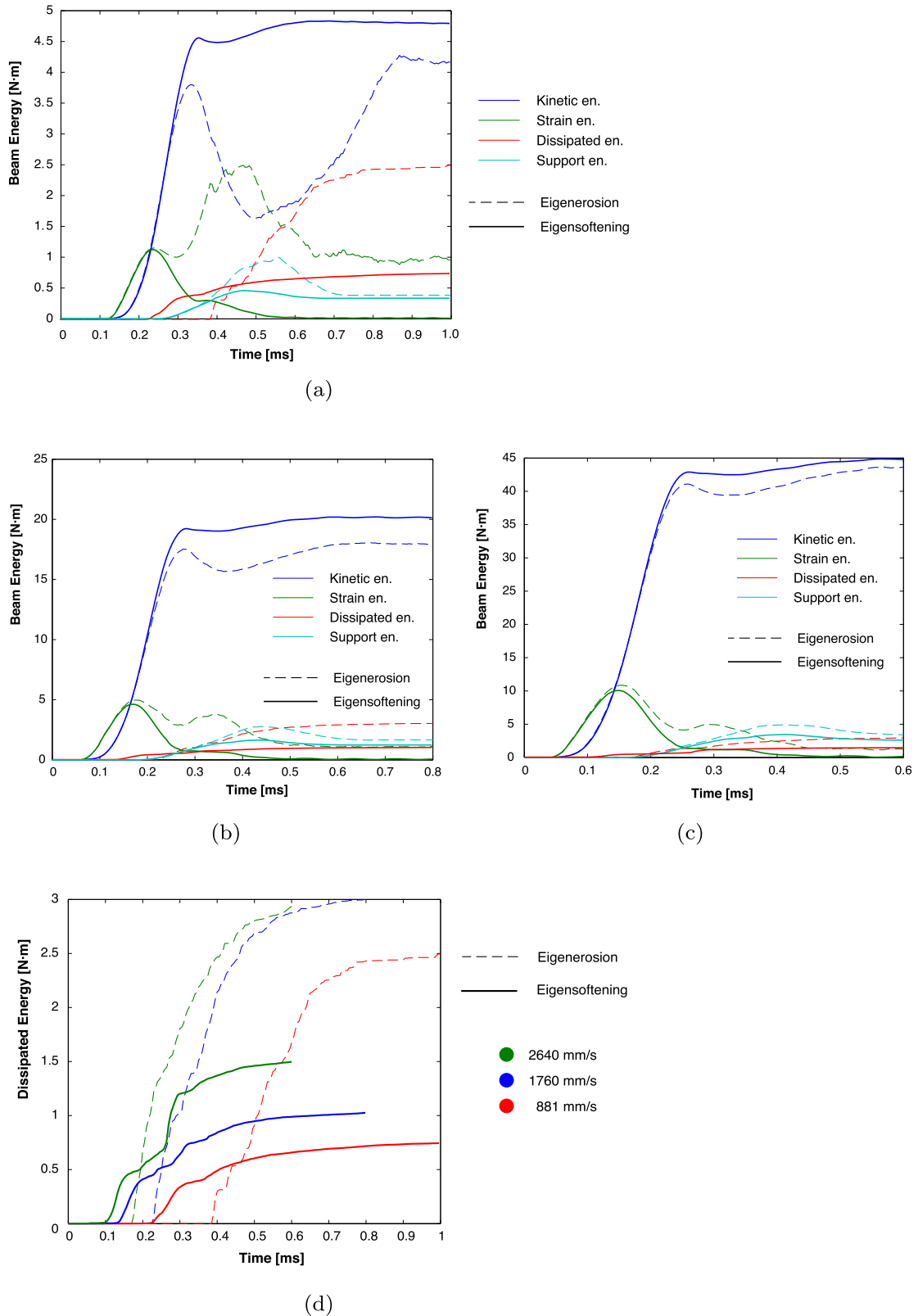
Fig. 10. Numerical energy evolution for both eigenerosion and eigensoftening methodologies for (a) 881 mm/s; (b) 1760 mm/s; and (c) 2640 mm/s; and (d) the zoomed view of the fracture energy expenditure.

the projectile and the beam during the impact process, observable from high-speed videos, is correctly captured. It is another evidence that the eigensoftening algorithm is suitable for modeling the fracture of quasi-brittle materials.

The second validation is carried out by comparing the strain history measured from the strain gauges with the numerical results obtained from both algorithms, see Fig. 6. Note that the results from the eigensoftening algorithm reproduce well both the general trend and the peak strains measured from the strain gauges, whereas those from the eigenerosion algorithm overestimate the peak strain values by a factor of close to ten.
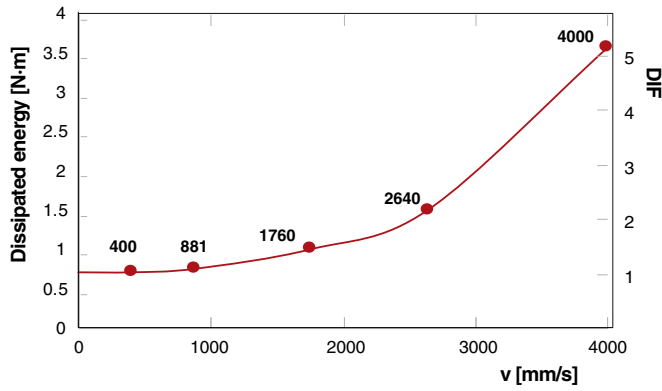
Fig. 11. Fracture energy dissipation and the corresponding DIF for impact velocities at 400, 881, 1760, 2640 and 4000 mm/s.
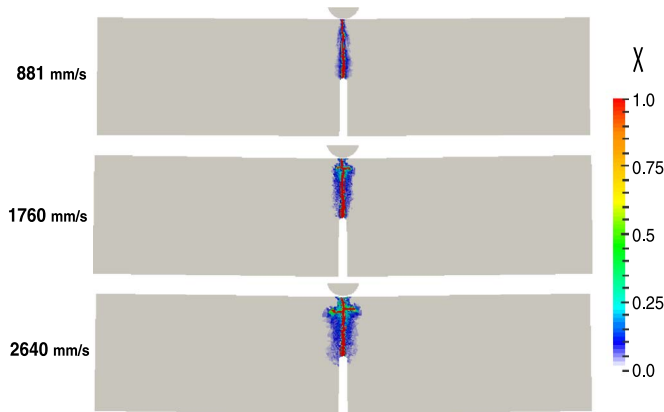

Fig. 12. Damage levels at the end of calculations for impact velocities at 881, 1760 and 2640 mm/s.

Table 3
Total damaged area, average damage and the total damaged area weighted with its χ values.

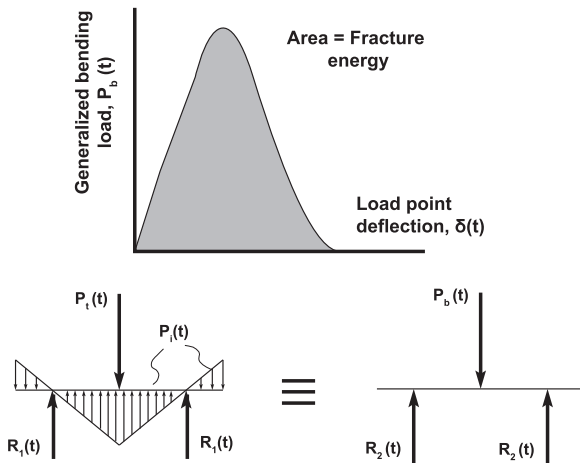|	ΣA_d [mm^2]	$\overline{\chi}$	$\Sigma \chi A_d$ [mm^2]
2640 mm/s	1385.6	0.222	307.4
1760 mm/s	822.7	0.290	240.4
881 mm/s	599.1	0.271	162.4

Fig. 13. Use the equivalent reaction (bending load) to calculate the fracture energy under dynamic loading (via a drop-weigh device).

4.2. Stress evolution and dynamic increase factor

In order to look at the dynamic effect on the stress amplitudes, we illustrate the stress distributions (in horizontal direction) at three time shots for all three impact velocities in Fig. 7. Note that even though the plotted stress range is limited between −10 and 10 MPa, significant higher values are observed for those results from the eigenerosion algorithm. Consequently, larger areas of stress concentration near the crack tip are perceived. Indeed, the dynamic increase factors (DIF) of the tensile stresses are 7.0, 8.2 and 8.5 for loading velocity at 881 mm/s 1760 mm/s and 2640 mm/s, respectively, see Fig. 8. By contrast, when eigensoftening is employed, the corresponding DIF for the tensile stresses reached only 1.14, 1.24 and 2.13 (see Table 2) for impact velocities of 881 mm/s 1760 mm/s and 2640 mm/s, respectively. These results together with the absolute values of the tensile stresses are also plotted in Fig. 8. It needs to be pointed out that, a DIF for tensile strength up to 1.8 was obtained by Beda et al. [29].

It is also worth noting that in Fig. 7 crack branches are formed for two higher impact velocities. This indicates that the excess energy supply is dissipated through creating more micro or macro cracks. Similar results were obtained on dynamic fracture propagation in concrete with rebars [30,31].

In order to gain more insights into the crack propagation velocities, the highest most recently eroded material points are extracted as crack fronts and plotted with respect to time in Fig. 9. Subsequently, derivatives are taken to obtain the crack propagation velocities. Note that the peak values of the crack velocity and the decreasing trend agree very well with the experimentally measured ones given by Zhang et al. [23] for both methods. Nevertheless, the crack speed obtained from eigensoftening are faster since it facilitates the crack initiation and propagation.

4.3. Energy evolution

Another interesting phenomenon is the quantification of fracture energy expenditure when inertia effects play an important role. In Fig. 10(a–c), the energy balance within the beam is presented for both eigenerosion and eigensoftening algorithms. Note that for all three impact velocities, kinetic energy is significantly higher than the rest, such as the strain energy, elastic energy at the two supports and the dissipated fracture energy. In the meantime, the general tendency from the eigensoftening model is the continuous increase of the kinetic energy and a decrease of the strain energy when fracture initiated.

In Fig. 10(d), the zoomed view of the amount of dissipated fracture energy is given. Note that for all three loading velocities, there is two or three times more fracture energy expenditure when eigenerosion is adopted. The dissipated fracture energy and the corresponding dynamic increase factor in G_F for the eigensoftening case is also plotted in Fig. 11 for two additional impact velocities, 400 and 4000 mm/s. It bears emphasis that at lower loading velocities, the dissipated fracture energy approaches to its static value 0.7 J (G_F multiplied by the area of the central section).

Fig. 12 describes the damage level achieved after the central crack has gone through the entire section. Note that the damage spreads to larger areas as the impact velocity increases. In other words, the dynamic increase in the fracture energy expenditure is attributed to more extended material failure. This can be verified by comparing the total damaged area, A_d, or its counterpart multiplied the corresponding damage values, χA_d. Consequently, the averaged damage, $\overline{\chi}$ can be calculated as:

$$\overline{\chi} = \frac{\sum \chi A_d}{\sum A_d}. \tag{18}$$

The three values for the three impact velocities are listed in Table 3. As expected, the total damaged area (with or without the weights of χ)
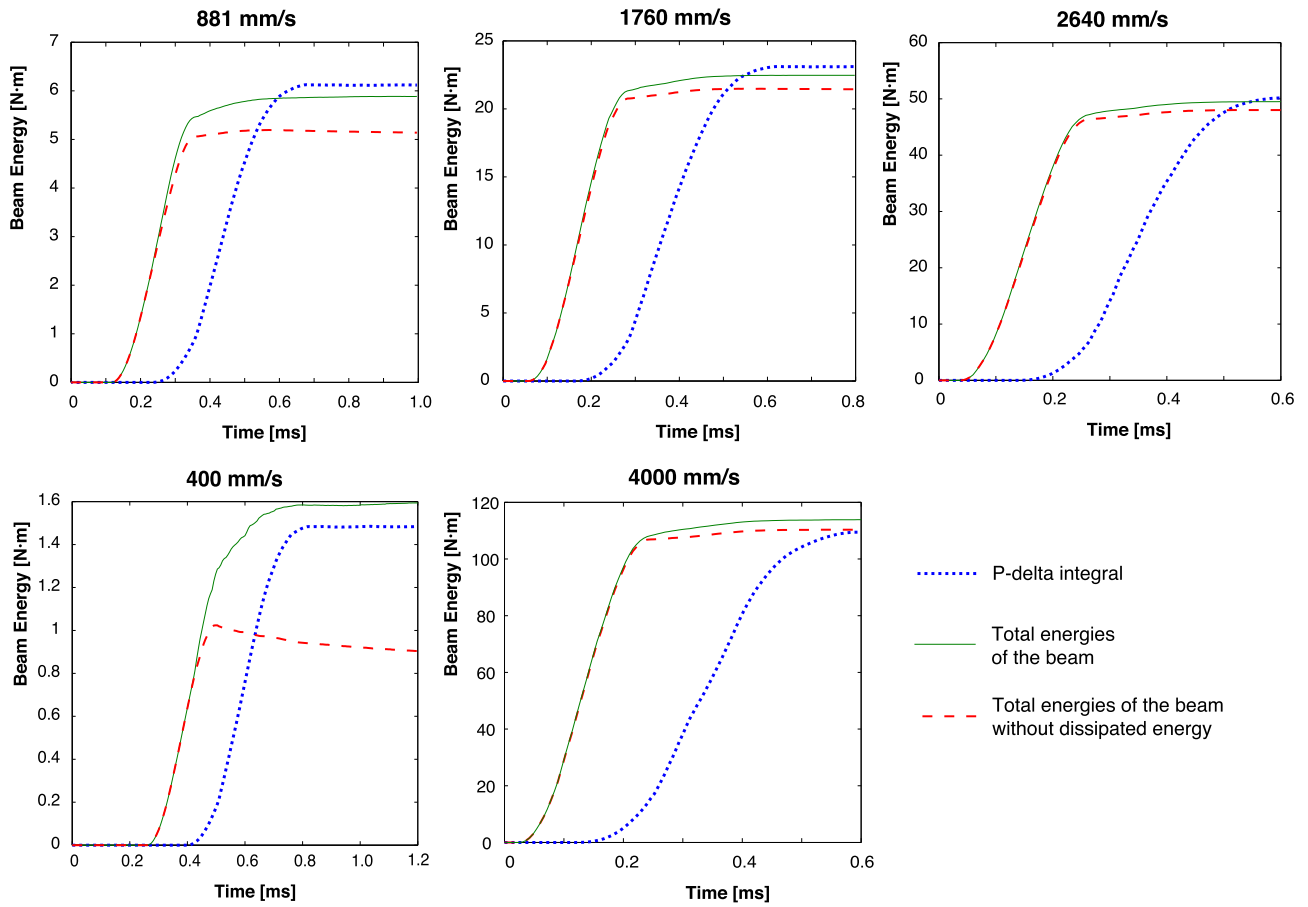
Fig. 14. Comparison of the beam energy with (green) or without (red) without the dissipated fracture energy with the integral of the P-delta curve (blue) for different impact velocities. (For interpretation of the references to colour in this figure legend, the reader is referred to the web version of this article.)
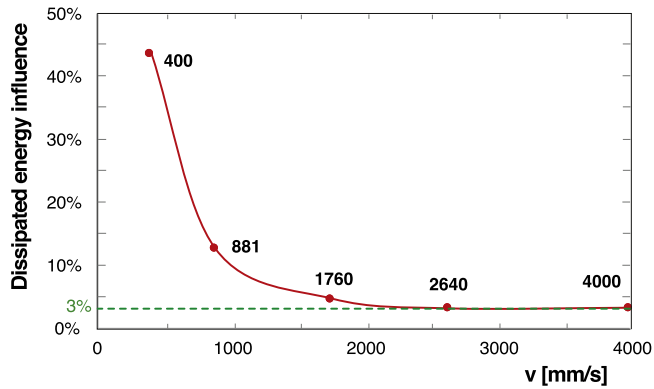

Fig. 15. Variation of the percentage of the dissipated fracture energy with respect to the total energy in the beam with the loading velocities.

grow with the impact velocity. Nevertheless, the average damage is independent of the loading rate. This indicates that the DIF in fracture energy is the result of failing more material points rather than more severely failing the same material. Similar conclusions were arrived in the work of Ruiz et al. [32] for the modelling of the failure of concrete cylinders through cohesive models.

4.4. Influence on the measurement of dynamic fracture energy

In order to experimentally measure the dynamic fracture energy, it is essential to take off the influence of inertia forces. Banthia et al. [18] proposed to employ the area below the reaction-deflection curve ($P - \delta$), see Fig. 13. In this Section, we endeavor to assess such a

procedure through the results from the aforementioned methodology with eigenerosion algorithm.

In Fig. 14, we plot the total energy of beam with (green solid lines) and without (red discontinuous lines) the dissipated energy contrasted with the $P - \delta$ integral (blue dotted lines). Note that there is insignificant difference between the green and blue curves for all five impact velocities considered. However, the difference between the red and green curves decreases with the impact velocity. In other words, the percentage of the dissipated fracture energy with respect to the total energy inside the beam decreases significantly with the increase of the impact velocity. This is clearly shown in Fig. 15. It is noteworthy that the area below the $P - \delta$ curve may indeed approaches the dissipated energy at static cases, in the dynamic case, however, it closely matches the total energy of the beam, whereas the fracture energy is solely a small percentage (3% when the impact velocity is higher than 2640 mm/s).

5. Summary and conclusions

Based on the eigenerosion approach to fracture, we have developed an eigensotening algorithm for the fracture of quasi-brittle materials. The former considers each material point can be either intact or be completely eroded. An energetic criterion is adopted for failure. The latter allows a gradual failure process of each material point, which is equivalent to a cohesive law in the context of cohesive fracture. A strength criterion is employed for crack initiation. Both methods are applied to model the dynamic fracture propagation in high-strength concrete through three-point-bend beams impacted at three different velocities. Even though the former is able to capture important features such as impact and reaction forces, the crack patterns, the predicted

values for stress and strains, however, are near ten times higher than the measured values. The eigensoftening algorithm instead, also reproduces correctly stress and strain values. We conclude that for quasi-brittle materials such as concrete, the eigensoftening approach to fracture may be used instead.

Making use of the eigensoftening algorithm, by modelling the hammer, the beam and the supports through contact, the energy balance between the projectile and the beam as well as the energy input from the supports are analyzed. It is demonstrated that the area below the reaction-deflection curve, employed in the hypothesis of Bathia et al., is an estimation of the total beam energy. The dissipated fracture energy is only a small percentage of the total energy when the impact velocity is high. Only at very low velocities or static case, the fracture energy expenditure can be approximated by the area below the reaction-deflection curve. This has to be taken into account if the dynamic fracture energy is to be measured through a drop-weight device.

Acknowledgments

Supplementary material

Supplementary material associated with this article can be found, in the online version, at 10.1016/j.ijimpeng.2017.11.004.

References

[1] Barenblatt G. The mathematical theory of equilibrium cracks in brittle fracture. Adv Appl Mech 1962;7:55–129.

[2] Hillerborg A, Modéer M, Petersson P. Analysis of crack formation and crack growth in concrete by means of fracture mechanics and finite elements. Cem Concr Res 1976;6:773–82.

[3] Ortiz M, Pandolfi A. Finite-deformation irreversible cohesive elements for three-dimensional crack-propagation analysis. Int J Numer Methods Eng 1999;44:1267–82.

[4] Pandolfi A, Ortiz M. An efficient adaptive procedure for three-dimensional fragmentation simulations. Eng Comput 2002;18(2):148–59.

[5] Ruiz G, Pandolfi A, Ortiz. M. Three-dimensional cohesive modeling of dynamic mixed-mode fracture. Int J Numer Methods Eng 2001;52:97–120.

[6] Bažant Z, Oh B. Crack band theory for fracture in concrete. Mater Struct 1983;16:155–77.

[7] Belytschko T, Chen H, Xu J, Zi G. Dynamic crack propagation based on loss of hyperbolicity and a new discontinuous enrichment. Int J Numer Methods Eng 2003;58:1873–905.

[8] Gravouil A, Moës N, Belytschko T. Non-planar 3D crack growth by the extended finite element and level sets-Part II: level set update. Int J Numer Methods Eng 2002;53:2569–86.

[9] Rabczuk T, Belytschko T. Cracking particles: a simplified meshfree method for arbitrary evolving cracks. Int J Numer Methods Eng 2004;61:2316–43.

[10] Schmidt B, Fraternali F, Ortiz M. Eigenfracture: an eigendeformation approach to variational fracture. SIAM J Multiscale Model Simul 2009;7:1237–66.

[11] Pandolfi A, Ortiz M. An eigenerosion approach to brittle fracture. Int J Numer Methods Eng 2012;92:694–714.

[12] Pandolfi A, Li B, Ortiz M. Modeling fracture by material-point erosion. Int JFract 2013;184:3–16.

[13] Li B, Pandolfi A, Ortiz M. Material-point erosion simulation of dynamic fragmentation of metals. Mech Mater 2015;80:288–97.

[14] Li B, Habbal F, Ortiz M. Optimal transportation meshfree approximation schemes for fluid and plastic flows. Int J Numer Methods Eng 2010;83:1541–79.

[15] Li B, Kadane A, Ravichandran G, Ortiz M. Verification and validation of the optimal-transportation meshfree (OTM) simulation of terminal ballistics. Int J Impact Eng 2012;42:25–36.

[16] Mindess S, Bentur A. A preliminary study of the fracture of concrete beams under impact loading, using high-speed photography. Cem Concr Res 1985;15(3):474–84.

[17] Mindess S, Banthia N, Yan C. The fracture-toughness of concrete under impact loading. Cem Concr Res 1986;17(2):231–41.

[18] Banthia N, Mindess S, Bentur A, Pigeon M. Impact testing of concrete using a drop-weight impact machine. Experimental Mech 1989;29(1):63–9.

[19] Banthia N, Mindess S, Trottier J. Impact resistance of steel fiber reinforced concrete. ACI Mater J 1996;93(5):472–9.

[20] Wang N, Mindess S, Ko K. Fiber reinforced concrete beams under impact loading. Cem Concr Res 1996;26(3):363–76.

[21] Banthia N, Yan C, Sakai K. Impact resistance of concrete plates reinforced with a fiber reinforced plastic grid. ACI Mater J 1998;95(1):11–8.

[22] Zhang X, Ruiz G, Yu R, Tarifa M. Fracture behaviour of high-strength concrete at a wide range of loading rates. Int J Impact Eng 2009;36:1204–9.

[23] Zhang X, Yu R, Ruiz G, Tarifa M, Camara M. Effect of loading rate on crack velocities in HSC. Int J Impact Eng 2010;37:359–70.

[24] Zhang X, Ruiz G, Yu R. A new drop-weight impact machine for studying fracture processes in structural concrete. Strain 2010;46(3):252–7.

[25] Ruiz G, Zhang X, Yu R, Porras R, Poveda E, del Viso J. Effect of loading rate on fracture energy of high-strength concrete. Strain 2011;47(6):518–24.

[26] Arroyo M, Ortiz M. Local maximum-entropy approximation schemes: a seamless bridge between finite elements and meshfree methods. Int J Numer Methods Eng 2006;65(13):2167–202.

[27] Navas P, López-Querol S, Yu R, Li B. B-bar based algorithm applied to meshfree numerical schemes to solve unconfined seepage problems through porous media. Int J Numer Anal Methods Geomech 2016;40:962–84.

[28] Bažant ZP, Planas J. Fracture and size effect in concrete and other quasi-brittle materials, New directions in Civil Engineering,. CRC Press, Boca Raton, Florida, USA; 1998.

[29] Beda N, Ozbolt J, Sharma A, Irhan B. Dynamic fracture of notched plain concrete beams: 3D finite element study. Int J Impact Eng 2015;77:176–88.

[30] Yu RC, Ruiz G. Modeling of static multi-cracking fracture processes in concrete using dynamic relaxation. Comput Concr 2004;4:371–88.

[31] Yu RC, Ruiz G. Explicit finite element modeling of static crack propagation in reinforced concrete. Int J Fract 2006;141:357–72.

[32] Ruiz G, Ortiz M, Pandolfi A. Three-dimensional finite-element simulation of the dynamic Brazilian tests on concrete cylinders. Int J Numer Methods Eng 2000;48:963–94.